Three-dimensional to two-dimensional transition in mode-I fracture microbranching in a perturbed hexagonal close-packed lattice

Shay I. Heizler[1,2,*] and David A. Kessler[1,†]
[1]*Department of Physics, Bar-Ilan University, Ramat-Gan, IL52900 Israel*
[2]*Department of Physics, Nuclear Research Center-Negev, P.O. Box 9001, Beer Sheva IL84190, Israel*
(Received 8 February 2017; revised manuscript received 7 May 2017; published 29 June 2017)

Mode-I fracture exhibits microbranching in the high velocity regime where the simple straight crack is unstable. For velocities below the instability, classic modeling using linear elasticity is valid. However, showing the existence of the instability and calculating the dynamics postinstability within the linear elastic framework is difficult and controversial. The experimental results give several indications that the microbranching phenomenon is basically a three-dimensional (3D) phenomenon. Nevertheless, the theoretical effort has been focused mostly on two-dimensional (2D) modeling. In this paper we study the microbranching instability using three-dimensional atomistic simulations, exploring the difference between the 2D and the 3D models. We find that the basic 3D fracture pattern shares similar behavior with the 2D case. Nevertheless, we exhibit a clear 3D-2D transition as the crack velocity increases, whereas as long as the microbranches are sufficiently small, the behavior is pure 3D behavior, whereas at large driving, as the size of the microbranches increases, more 2D-like behavior is exhibited. In addition, in 3D simulations, the quantitative features of the microbranches, separating the regimes of steady-state cracks (mirror) and postinstability (mist-hackle) are reproduced clearly, consistent with the experimental findings.

DOI: 10.1103/PhysRevE.95.063004

I. INTRODUCTION

Over the past decades, the dynamic instability in mode-I fracture has been studied extensively [1]. These findings deviate from the two-dimensional (2D) classic model for mode-I fracture with a single crack that propagates in the midline of the sample, based on linear elasticity fracture mechanics (LEFM) [2]. This classic theory, which lacked a supplemental criterion for instability, predicts that a single crack will accelerate to a terminal velocity, which for mode-I fracture is the Rayleigh surface wave speed c_R. In fact, as long as a single crack does exist, the crack obeys LEFM predictions [3,4]. However, the experiments find that at a much lower velocity (≈ 0.36–$0.42c_R$, for a short review, see, for example, Ref. [5]), a dynamic instability occurs, and small microbranches start to appear near the main crack [6–10]. The additional energy that has to be spent in creating the new surfaces prevents the crack from accelerating to the theoretical terminal velocity. LEFM-based universal criteria for branching [11,12] fail to describe the instability, predicting a much higher critical velocity than in reality. Moreover, when the small microbranches appear at $v \geqslant v_{\rm cr}$, they present a clear three-dimensional (3D) nature. However, when enlarging the driving displacement, the small microbranches reunite, creating 2D patterns (right before macrobranches appear), especially in poly(methyl methacrylate) (PMMA) [7–10].

Lattice models reproduce the existence of steady-state cracks [13,14], and via a standard linear stability analysis, they predict the existence of a critical velocity when the steady-state cracks become linearly unstable [15–19]. This critical velocity is found to be strongly dependent on the details of the interatomic potential, such as the degree of smoothness of the potential (as it drops to zero), or the amount of dissipation. Simple simulations that use these same potentials succeed in reproducing the steady-state regime, yielding the exact point of instability and in reproducing the lattice model results, but fail to describe the behavior in the postinstability regime [18,20]. The early efforts on using a binary-alloy model for modeling brittle amorphous materials failed to achieve steady-state cracks at all [21], although more recent attempts have succeeded in yielding propagating cracks [22,23].

Recent studies using Zachariasen's [24] 2D continuous random network model of amorphous materials, a model that also recently has received experimental support from direct imaging of 2D silica glasses [25], were used in describing the microbranching instability [26] [using a $O(10^4)$ 2D particle mesh]. The simulations reproduced qualitatively both the regime of the steady-state propagating cracks and the fracture patterns of the microbranches. In addition, using perturbed lattice models, generated by adding a small amount of disorder to the bond lengths, supplemented by an additional three-body force law which penalizes the rotation of the bonds away from the natural directions of the lattice, produces similar results [27]. Larger-scale simulations [$O(10^6)$ particles] using graphics processing unit (GPU) computing yields various qualitative and quantitative results of postinstability behavior, such as a sharp transition between the regime of the steady state and the microbranching, the increase in the derivative of the electrical resistance across the crack with respect to time (which correlates experimentally with the crack velocity), the correct branching angle, and the power-law behavior of the branch shapes [28]. All of the theoretical models that were mentioned above employed a 2D description of the problem.

The large-scale simulations allow us to perform 3D simulations, attacking the microbranching phenomenon which

*highzlers@walla.co.il
†kessler@dave.ph.biu.ac.il

is, at its heart, a 3D phenomenon [1,8,29], by taking the $O(10^4)$ particle mesh and adding a third dimension with $N_Z \approx 100$. The two basic questions that we address using our 3D simulations are as follows:

(i) Checking the reliability of the previous 2D simulations, investigating how well the 2D description reproduces the behavior of the more realistic 3D models.

(ii) Studying the direct 3D experimental features of the microbranches, which have not previously been modeled.

We note that several 3D fracture molecular-dynamics simulations, containing large numbers of atoms, have been studied previously using different potentials (for example, see Refs. [30–32]), but herein we focus on the features of the 3D instability and the resulting microbranches. It is important to note that atomistic simulations cannot reproduce the fracture patterns on the real physical length scales of the experiments. However, the aim is to reproduce *scaled* results and scaled structures of the real fracture length scales.

II. MODEL AND GENERAL METHODOLOGY

Our simulations consist of $\approx 3 \times 10^6$ atoms, which include 1.7×10^7 bonds (central force laws), and $\approx 3.4 \times 10^7$ three-body interactions (see Appendix B for the exact parameter of the three-body potential that was used). These simulations can be performed in reasonable run times by using parallel GPU computing (see Appendix C).

We used a perturbed hexagonal close-packed (hcp) structure, which is a 3D extension of the 2D perturbed hexagonal lattice that was studied in Refs. [27,28]. As in our 2D studies, the interactions are taken to be only between nearest neighbors in the unperturbed hcp lattice with an in-plane lattice constant of $a = 4$ and $c = \sqrt{8/3}a$ (see Fig. 9 in Appendix A). Every atom has 12 closest neighbors. We add a small amount of disorder to the bond lengths $a_{i,j} = (1 + \epsilon_{i,j})a$ where $\epsilon_{i,j} \in [-b,b]$ and b is constant and in this paper is set to $b = 0.1$ (for the system shape, see Fig. 10 in Appendix B). In most of our simulations, we employed a piecewise-linear radial force law (in this paper, $k_r = 1$) between the initially neighboring atoms. However, in some of them we used a more physical smooth force law using a smoothness parameter α, which when $\alpha \to \infty$ reproduces the piecewise-linear model (see Appendix B). In addition, we add a three-body potential and Kelvin-type viscosity as described in detail in our 2D lattice studies [27,28]. We relax the system, and then we strain the lattice under a mode-I tensile loading with a given constant strain grip boundary condition corresponding to a given driving displacement $\pm\Delta$ (which is normalized relative to the Griffith displacement Δ_G) of the edges and seed the system with an initial crack. For a detailed discussion regarding the model and the governing equations, see Appendixes A and B. The crack then propagates via the same molecular-dynamics Euler scheme (the simulations were always stable using a reasonable value of dt, so we have not needed any more sophisticated numerical schemes). In Fig. 1 we present close-in snapshots of the (same) crack tip in a steady-state crack from different viewing angles. We can see that at small driving displacement the crack is actually 2D in nature.

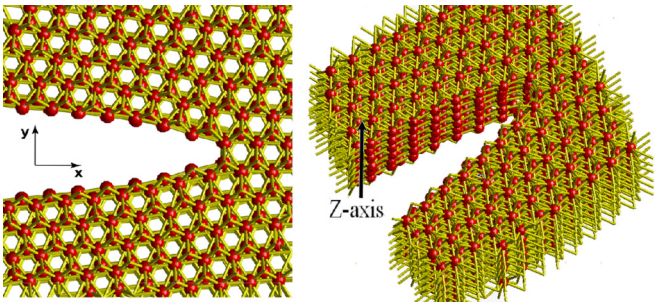

FIG. 1. A snapshot of the (same) crack tip in a steady-state crack using a perturbed hcp lattice from different viewing angles. Each atom shares 12 nearest neighbors (nns), defining "bonds" that connect each other by a force law and is allowed to move in all three coordinates. The crack creates a mirrorlike pattern. The left snapshot is a clear XY-plane view whereas the right has a slight tilt, showing how deep the system is.

III. MICROBRANCHING INSTABILITY IN A 3D-PERTURBED LATTICE

The crack velocity v (which we normalize to the Rayleigh wave speed c_R) increases with Δ/Δ_G (see Fig. 2). We define the Rayleigh wave speed here as that calculated from c_l and c_t (the longitude and the transverse wave speeds) on the XY plane [(0001) in the crystallographic notation], which is the major fracture surface in our simulations (there is a symmetry along the Z axes in steady-state cracks, see Appendix C). We can see that using a perfect nonperturbed lattice (in these simulations we also used $k_\theta = 0$ in addition to $b = 0$, but this result is valid for all values of k_θ), we get a (nonphysical) velocity gap (such as in 2D [15–18]) in which slow cracks are prohibited. However, adding disorder and the three-body force law, the velocity gap shrinks, and by using a finite value of α, the velocity gap shrinks dramatically with steady-state cracks with almost zero velocities, yielding the correct experimental behavior [1].

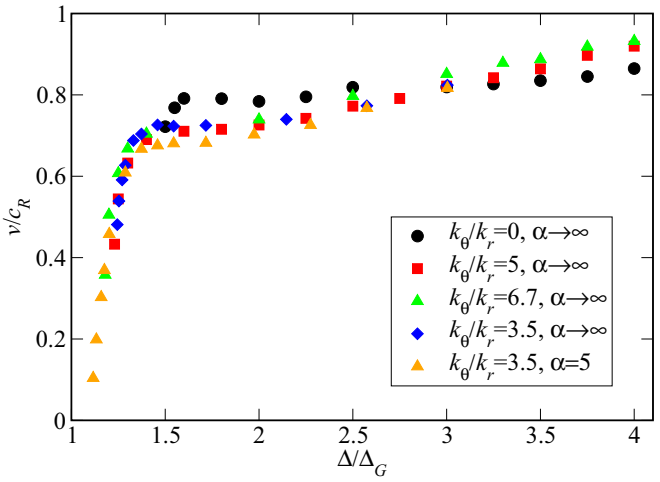

FIG. 2. The $v(\Delta)$ curve of the perturbed hcp with different values of two-body and three-body force laws. With a finite value of α and k_θ/k_r, the velocity gap shrinks dramatically, yielding the correct experimental behavior.

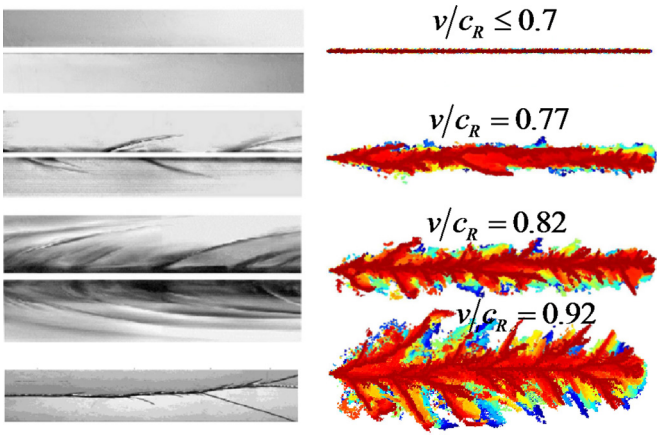

FIG. 3. An XY-plane view of the experimental microbranching phenomenon in PMMA taken from Refs. [8,10] (left) for increasing driving displacement. In color (right) we see our simulation XY-plane view where the color denotes the Z location of the broken bonds (dark red for the top edge and dark blue for the bottom edge). We can see that, despite the quite noisy simulations, in general the qualitative picture is quite good. The upper picture yields a mirrorlike steady-state crack and is valid for all $v/c_R \leqslant 0.7$.

In Fig. 3 we show several microbranching patterns (top views), both experimental (in PMMA) and from our 3D simulations using $k_\theta/k_r = 5$ (where the color denotes the Z locations). The broken bonds are plotted in the fractured system, and their Z locations can be associated with the color where dark red represents the top edge and dark blue stands for the bottom edge. We see that below the critical velocity, in the regime of steady-state cracks, the crack has a "mirror" surface. Increasing the driving displacement, small microbranches appear nearby the main crack, whereas the sizes of the microbranches increase dramatically with the driving, yielding at first a "mist" surface and with large Δ, a "hackle" surface. Despite the noisy results (due to the relatively small sizes of the simulations), the pictures are qualitatively quite similar to the experimental findings, at least in the sense that the length of the microbranches increases dramatically with the driving displacement, yielding eventually large macrobranches (in the simulations, a macrobranch is a branch that reaches the end of the sample, such as in the experiments, on a different length scale). A quantitative (scaled) overview is presented in Figs. 4 and 5. We note that without a three-body force law we do not get the microbranching pattern, but rather a cleavagelike behavior (with or without the presence of disorder). Using too strong a three-body force law ($k_\theta/k_r = 6.7$) yields microbranches that propagate in straight lines with the natural angle of the lattice (60°), which is again nonphysical.

The transition between the regime of steady-state cracks and the postinstability side-branching regime is very sharp in the 3D simulations. In Figs. 4 and 5 we present two quantitative parameters that demonstrate this sharp transition (in the inset there is a zoomed picture of the transition area). In Fig. 4 the total number of broken bonds as a function of the crack velocity is displayed. In the small velocity regime, only the bonds necessary for yielding a single main crack are broken.

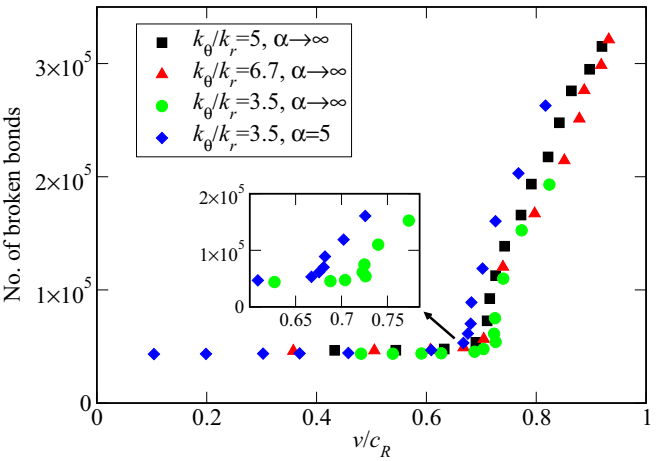

FIG. 4. The total number of broken bonds as a function of the crack velocity (the constant number of bonds in the low velocity regime represents the broken bonds of the main crack). A clear transition between the steady-state regime and the microbranching behavior can be seen. In the small box there is a zoomed picture of the transition area.

Beyond the critical velocity, the number of broken bonds increases linearly as in the experiments [8] and is broadly similar (although much sharper here) to what is seen in the hexagonal perturbed 2D lattice [28].

In Fig. 5 we measure δy, the width of the microbranching region, as a function of the crack velocity (see the definition inside Fig. 5). δy is a second measure of the sizes of the microbranches. As above, a sharp transition can be seen between the single crack and the microbranching regimes. We note that using the piecewise-linear force law, the critical velocity $v_{\rm cr}$ seems to be very close to the Yoffe criterion [11] (which is $\approx 0.73 c_R$). But, as we showed previously in 2D, the quantitative value of $v_{\rm cr}$ can be controlled via the interatomic potential parameters, such as α and η (see Appendix B for explicit definitions of these parameters) [16,18,28]. We

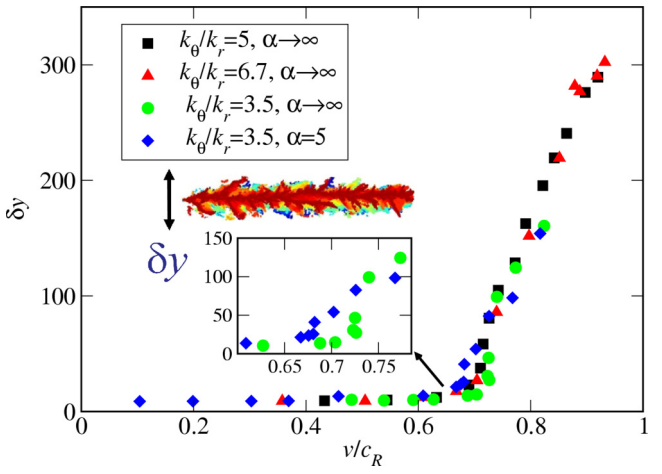

FIG. 5. The width of the fracture region as a function of the crack velocity. A clear transition between the steady-state regime and the microbranching behavior can be seen. In the small box there is a zoomed-in picture of the transition area.

can see that using a finite value of α, the critical velocity decreases (see the small boxes in Figs. 4 and 5 for a given k_θ) to the exact value of the 2D simulations; in $\alpha \to \infty$ we reproduce the 2D critical velocity $v_{\rm cr} \approx 0.73 c_R$ (see Fig. 7 in Ref. [17]), whereas also with $\alpha = 5$ we reproduce the 2D value $v_{\rm cr} \approx 0.68 c_R$ (see Fig. 4(a) in Ref. [18]). That means that the critical velocity is not universal and is potential dependent. Thus, for example, we can vary the values of α and η to reproduce the exact experimental critical velocity of a given material, very much like we did in 2D [18,19]. In both Figs. 4 and 5, the results appear insensitive to the exact value of k_θ, despite the fact that the microbranches in the two cases appear different.

In addition, we can cut thin horizontal slices from the XY fracture pattern, yielding 2D patterns and compare them to pure 2D fracture patterns [27]. In Fig. 6 we present two fracture patterns of a 2D perturbed hexagonal lattice and two 2D slices of the 3D hcp perturbed lattice, one for relatively small driving and one for large driving displacement. We can see, despite the relatively large noise (resulting from the breaking of one or a few bonds) that characterizes the 3D simulations, the patterns are quite similar to the pure 2D simulations for small driving displacement. This fact is encouraging and supports the assumption that for at least some features (e.g., XY-plane features of the microbranches), the 2D studies are relevant. However, for large driving displacement, the 3D patterns look rather different from the 2D patterns, although the fracture pattern is still much more developed at large driving displacements. Nevertheless, we note that different horizontal slices of the same 3D fracture pattern (for different Z's) yield different patterns. This fact indicates that, for the 3D regime, as long as the microbranches are sufficiently small, there is no symmetry along the Z axis. Note that the driving displacement v/c_R required to produce a given amount of side branching is much greater than in 2D since out of plane bonds are being broken as well.

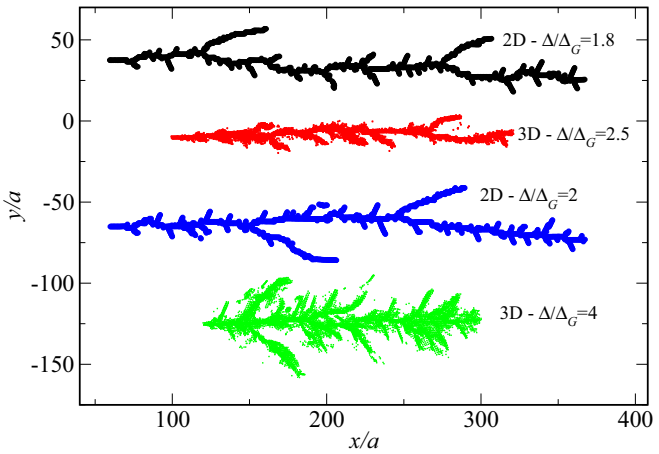

FIG. 6. A comparison between the fracture pattern (in lattice scale units) of a pure 2D perturbed hexagonal simulation and the thin slices of the 3D fracture pattern using our perturbed hcp lattice. Despite the greater noise of the 3D simulations, the patterns look quite similar. The 2D patterns are taken from Ref. [27].

IV. THE 3D-2D TRANSITION

Moreover, we can compare our 3D simulations to the 3D experimental properties of the microbranches. Experimental postmortem pictures of the XZ plane of the fractured surface by Sharon and Fineberg [8] reveal that, nearby the origin of instability, the microbranches are localized on the Z axis. At high velocities, the microbranches merge, creating a Z-plane quasisymmetric pattern, yielding a 3D-2D transition [1,8–10]. In PMMA (as opposed to glasses or gels), nice symmetric 2D-like stripes are created in association with the largest microbranches [8].

In Fig. 7 we present two experimental pictures of the XZ plane of the fracture surface that demonstrates the 2D-3D transition in PMMA, taken from Ref. [8]. Below, we depict XZ slices taken at a constant distance from the main crack (relative to the Y axis) of our 3D simulations (the pictures from the main crack plane itself are too noisy due to our finite size simulations). We see that the fracture patterns looks surprisingly similar. At a small driving displacement ($\Delta/\Delta_G = 2.5$ in the simulations), right beyond the critical velocity, the microbranches are localized in the Z directions, yielding purely 3D behavior in both the experiments and the simulations. Increasing the driving displacement further ($\Delta/\Delta_G = 4$ in the simulations), the microbranching increases in the Z direction from top to bottom of the sample, yielding a 2D-type behavior. The periodic stripes structure is a result of the periodic microbranches on the XY plane (Fig. 3) [7]. After the onset of branching, the energy flowing into the crack tip is divided between the main crack and the daughter cracks. The daughter cracks, which compete with the main crack, have a finite (similar) lifetime because the main crack can outrun them and screen the daughter cracks from the surrounding stress field. The daughter cracks then die, and the energy that had been diverted from the main crack returns. The scenario then repeats itself, causing the branching pattern to be more or less periodic.

As a matter of fact, these large microbranches result from the merging of several small microbranches as we can see

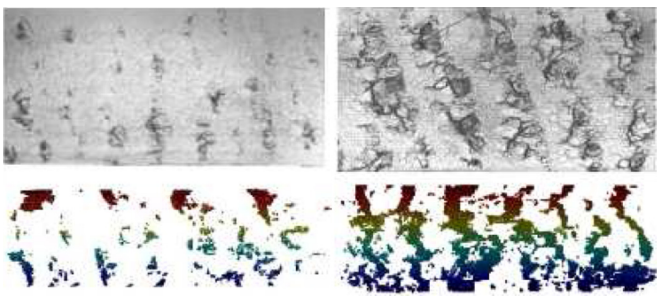

FIG. 7. Top row: an XZ-plane view of the experimental microbranching phenomenon in PMMA of the Sharon and Fineberg experiments (which are taken from Ref. [8]), along with simulation results (where the color denotes the Z location of the broken bonds for presentation reasons) for small driving on the left and for large driving displacement on the right. Bottom row: the simulational XZ-plane view. We see that very much like the experiments, at the small driving displacement, the microbranching is 3D, and for the large driving displacement, the microbranches are 2D in character.

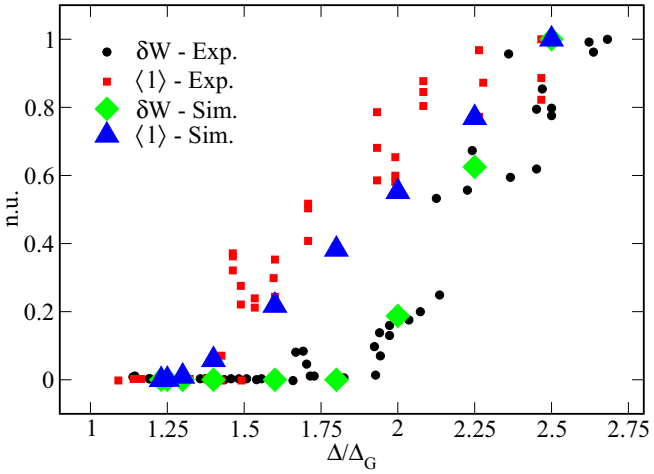

FIG. 8. A comparison between experimental and simulation results for the average length of the microbranch and the microbranch width (normalized to the maximal yielded value) as a function of the driving displacement (normalized to the Griffith value). The experimental data are taken from Refs. [1,8].

carefully in Fig. 7 (there is not a perfect symmetry along the Z axis; for different Z's, the microbranch propagates different distances). This behavior shares similar features with recent experimental work [29].

We can now quantify this 2D-3D transition (of course in normalized units). Looking carefully at the PMMA experimental results, we can see that the region of instability $v = v_{\rm cr} \approx 340$ m/s (Fig. 11(a) in Ref. [8]) is quite different from the point of 2D-3D transition $v \approx 550$ m/s (Fig. 19 in Ref. [8]), ensuring the fact that at first (near $v \approx v_{\rm cr}$) the microbranches are 3D whereas only for higher velocities do they become 2D. In Fig. 8, we plot the width of the largest microbranch (in the Z direction) in the 3D simulations for a given Δ/Δ_G along with the total number of broken bonds (from Fig. 4), both of them are normalized to their largest value. We plot them both as a function of Δ/Δ_G and not as a function of v/c_R since the crack velocities are an output parameter (and in our simulations are much higher than the PMMA experimental results). For the experimental results, we used Fig. 17 in Ref. [1] for transferring the data from v/c_R to Δ/Δ_G.

We can see that the 3D simulation results reproduce the 2D-3D transition almost perfectly. At $\Delta/\Delta_G \approx 1.3$, in both the experimental and the simulation results, small microbranches start to appear on the main crack. Those microbranches are localized in the Z direction, whereas only at $\Delta/\Delta_G \approx 1.8$–$1.9$ does the width of the microbranches increase dramatically, yielding "2D microbranches" when several microbranches reunite, covering the whole Z direction, yielding a 3D-2D transition.

V. SUMMARY AND FUTURE WORK

In conclusion, as long as we look at the XY plane, the 3D simulations share similar features with the 2D simulations, and quantitative measures as to the total number of microbranches or the size of the opening of the microbranches as a function of crack velocity look the same. On the other hand, our current simulations also reproduce pure 3D features, especially the XZ-plane patterns when the 3D-2D transition occurs. Thus, we believe that the lattice models and simulations offer a good theoretical framework for studying the microbranching instability, including the 3D effects. We are left with the following question. In 2D [28], enlarging the system allows quantitative study of the branches. How will the 3D system behave on a larger scale? The answers should be attainable within the scope of available supercomputers using thousands of nodes or tens of GPUs.

APPENDIX A: GENERATING THE PERTURBED LATTICE

We start with a perfect ideal hcp lattice, where $c = \sqrt{8/3}a$ (see Fig. 9) when each atom has 12 nearest neighbors, 6 on the XY plane (yielding a 2D hexagonal lattice) and 6 in the Z direction (3 up and 3 down). As in the 2D studies [27,28], we randomize the length of each bond $a_{i,j}$,

$$a_{i,j} = (1 + \epsilon_{i,j})a, \quad i = 1,2,\ldots,n_{\rm atoms}, \quad j \in \mathcal{N}(i), \quad \text{(A1)}$$

where $\epsilon_{ij} \in [-b,b]$ and b is constant for a given lattice. In this paper we set $b = 0.1$ and $a = 4$. $\mathcal{N}(i)$ refers to the nearest neighbors of site i.

APPENDIX B: THE EQUATIONS OF MOTION

In most of our calculations, between each two atoms there is a piecewise-linear radial force (two-body force law) of the form

$$\vec{f}^{\,r}_{i,j} = k_r k'_{i,j}(|\vec{r}_{i,j}| - a_{i,j})\hat{r}_{j,i}, \quad \text{(B1)}$$

where

$$k'_{i,j} \equiv \theta_H(\varepsilon - |\vec{r}_{i,j}|). \quad \text{(B2)}$$

The Heaviside step function θ_H guarantees that the force drops immediately to zero when the distance between two atoms $|\vec{r}_{i,j}|$ reaches a certain value of $\varepsilon > a_{i,j}$ (the breaking of a bond). In this paper we set $\varepsilon = a + 1$. Alternatively to Eq. (B2), we can use a smoother force law, which, instead of a sharp failure at $|\vec{r}_{i,j}| = \varepsilon$, has a more realistic smooth transition wherein the force law drops to zero, of the form [16,18]

$$k'_{i,j} \equiv \frac{1 + \tanh[\alpha(\varepsilon - \vec{r}_{i,j})]}{1 + \tanh(\alpha)}, \quad \text{(B3)}$$

where α is the smoothness parameter such that when $\alpha \to \infty$ the force law reverts to the piecewise-linear force law. The results in this paper refer to the piecewise-linear model, unless mentioned otherwise.

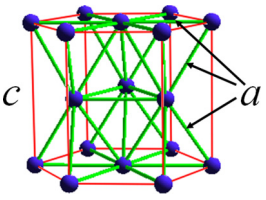

FIG. 9. A diagram of the unit cell of the ideal hcp lattice, where $c = \sqrt{8/3}a$. Each atom has 12 nearest neighbors, 6 on the XY plane (reproducing the 2D hexagonal lattice).

In addition there is a three-body force law that depends on the cosine of the angles between each set of three neighboring atoms, defined of course by

$$\cos\,\theta_{i,j,k} = \frac{\vec{r}_{i,j}\cdot\vec{r}_{i,k}}{|\vec{r}_{i,j}||\vec{r}_{i,k}|}, \tag{B4}$$

that acts on the central atom (atom i) of each angle and may be expressed as

$$\begin{aligned}\vec{f}^{\,\theta}_{i,(j,k)} &= k_\theta(\cos\,\theta_{i,j,k} - \cos\,\theta_C)\frac{\partial\cos\,\theta_{i,j,k}}{\partial\vec{r}_i}k'_{i,j}k'_{i,k}\hat{r}_i \\ &= k_\theta(\cos\,\theta_{i,j,k} - \cos\,\theta_C) \\ &\quad\times\left[\frac{\vec{r}_{i,j}+\vec{r}_{i,k}}{|\vec{r}_{i,j}||\vec{r}_{i,k}|} + \frac{\vec{r}_{j,i}(\vec{r}_{i,j}\cdot\vec{r}_{i,k})}{|\vec{r}_{i,j}|^3|\vec{r}_{i,k}|} + \frac{\vec{r}_{k,i}(\vec{r}_{i,j}\cdot\vec{r}_{i,k})}{|\vec{r}_{i,j}||\vec{r}_{i,k}|^3}\right] \\ &\quad\times k'_{i,j}k'_{i,k},\end{aligned} \tag{B5}$$

whereas the force that is applied on the other two atoms (atoms j,k) may be expressed as

$$\begin{aligned}\vec{f}^{\,\theta}_{j,(i,k)} &= k_\theta(\cos\,\theta_{i,j,k} - \cos\,\theta_C)\frac{\partial\cos\,\theta_{i,j,k}}{\partial\vec{r}_j}k'_{i,j}k'_{i,k}\hat{r}_j \\ &= k_\theta(\cos\,\theta_{i,j,k} - \cos\,\theta_C) \\ &\quad\times\left[\frac{\vec{r}_{k,i}}{|\vec{r}_{i,j}||\vec{r}_{i,k}|} + \frac{\vec{r}_{i,j}(\vec{r}_{i,j}\cdot\vec{r}_{i,k})}{|\vec{r}_{i,j}|^3|\vec{r}_{i,k}|}\right]k'_{i,j}k'_{i,k}.\end{aligned} \tag{B6}$$

Of course, the forces satisfy the relation $\vec{f}^{\,\theta}_{i,(j,k)} = -(\vec{f}^{\,\theta}_{j,(i,k)} + \vec{f}^{\,\theta}_{k,(i,j)})$. The three-body force law drops immediately to zero when using a piecewise-linear force law when the bond breaks [Eq. (B2)] or may be taken to vanish smoothly using Eq. (B3).

We note that, in the 3D case, there are a lot of possible angles between each set of three bonds. To shorten the run times (the calculation of the three-body force law is extremely time consuming), in most of our calculations, we do not include all the possible angles between triplets but only 12 of them. We chose to take the six 60° angles inside the XY plane (for reproducing the 2D-hexagonal problem that was studied before for $N_z = 1$) and another six angles, three 60° angles that connect each atom with its two neighbors that are located on the upper parallel plane and three angles on the lower parallel plane (for convenience, see Fig. 9). However, in some of our calculations, we used all twenty-four 60° angles, whereas the results do not vary qualitatively, and the fracture patterns remain similar. There is a certain preferred angle θ_C for which the three-body force law vanishes, which is set to $\theta_C = \frac{\pi}{3}$.

In addition, it is convenient to add a small Kelvin-type viscoelastic force proportional to the relative velocity between the two atoms of the bond $\vec{v}_{i,j}$ [16–18,33],

$$\vec{g}^{\,r}_{i,j} = \eta(\vec{v}_{i,j}\cdot\hat{r}_{i,j})k'_{i,j}\hat{r}_{i,j}, \tag{B7}$$

with η as the viscosity parameter. The viscous force vanishes after the bond is broken, governed by $k'_{i,j}$. The imposition of a small amount of such a viscosity acts to stabilize the system and is especially useful in the relatively small systems simulated herein.

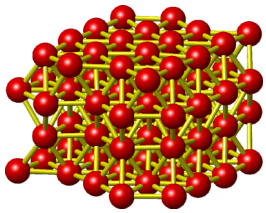

FIG. 10. A small-scale perturbed hcp yielded by Eq. (A1) after relaxing the system under Eqs. (B1)–(B8).

The set of equations of motion of each atom is then

$$m_i\ddot{\vec{a}}_i = \sum_{j\in 12\,\mathrm{nn}}\left(\vec{f}^{\,r}_{i,j} + \vec{g}^{\,r}_{i,j}\right) + \sum_{j,k\in 12\,\mathrm{nn}}\vec{f}^{\,\theta}_{i,(j,k)} + \sum_{j\in 24\,\mathrm{nn}}\vec{f}^{\,\theta}_{j,(i,k)}. \tag{B8}$$

In this paper the units are chosen so that the radial spring constant k_r and the atoms' mass m_i are unity.

After defining the steady-state optimal length of each bond $a_{i,j}$ by Eq. (A1), we first relax the system under the equations of motion, Eqs. (B1)–(B8) with a small amount of viscosity, yielding the minimal-energy locations of the atoms in the lattice. In Fig. 10, we can see a small-scale 3D perturbed hcp using our model.

After relaxing the initial lattice, we strain the lattice under a mode-I tensile loading with a given constant strain corresponding to a given driving displacement $\pm\Delta$ of the edges and seed the system with an initial crack. The crack then propagates via the same molecular-dynamics Euler scheme using Eqs. (B1)–(B8).

APPENDIX C: PARALLELIZATION BY GPU COMPUTING

As mentioned in Secs. I and II, running 3D simulations, using approximately 3×10^6 particles cannot reasonably be performed by a single CPU and thus force us to use multithread computing. We choose to use GPU computing, parallelizing the code via CUDA [34,35], akin to what we implemented before in 2D [28]. This kind of programming forces the programmer to use the different levels of memory carefully [35], which makes achieving an acceleration up to ≈100 faster than a regular C code possible using a single CPU. This tool makes the simulation of millions of atoms in reasonable simulation times possible. See the Appendix of Ref. [28] for more implementation details. In our simulations, we used $132\times310\times70\approx3\times10^6$ particles ($N = 65$ in the Slepyan model notation).

APPENDIX D: THE RAYLEIGH SURFACE WAVE SPEED FOR HCP WITH $k_\theta \neq 0$ LATTICES

Since the models in this paper use a three-body potential law (aside the central two-body force law) with $k_\theta \neq 0$, we need to recalculate the Rayleigh wave speed c_R, which is the terminal velocity for mode-I fracture for different k_θ/k_r's. The most convenient way to calculate the Rayleigh wave speed is to calculate first the longitude (primary) c_l and the transverse (secondary) c_t wave speeds and then to calculate the Rayleigh

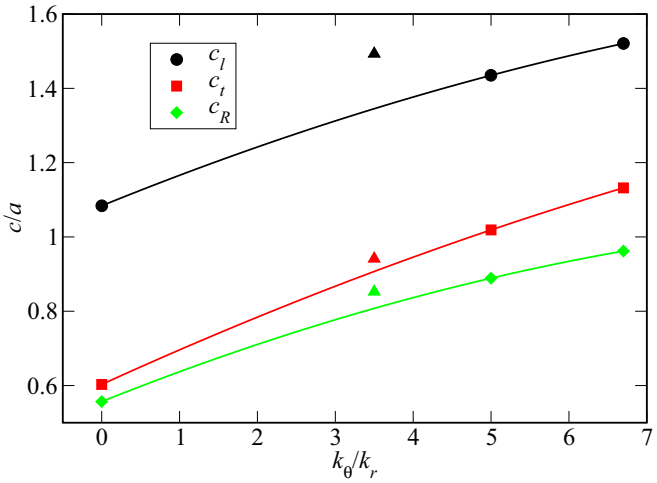

FIG. 11. The longitude and the transverse sound wave speeds along with the resulting calculated Rayleigh surface wave speed using Eq. (D1) for the hcp lattice as a function of k_θ/k_r. In the circles there are the results with only twelve 60° angles that were taken into account, whereas in the triangles, the result is with all twenty-four 60° angles.

wave speed via the well-known formula [36],

$$\left(1-\frac{c_R^2}{c_t^2}\right)^2-4\left(1-\frac{c_R^2}{c_l^2}\right)^{1/2}\left(1-\frac{c_R^2}{c_t^2}\right)^{1/2}=0. \qquad \text{(D1)}$$

Since in a hcp lattice, the sound velocities are inhomogeneous, yielding a different sound velocity for each direction, we defined that the relevant variables are the variables on the XY plane, which is the major fracture plane, and thus, the crack velocities are normalized to the sound velocities on the XY plane (which inside this plane, are homogeneous, as for a 2D hexagonal lattice). In this manner we define the Rayleigh wave speed on the XY plane by Eq. (D1). We calculate c_l and c_t via measuring the wave velocities by initiating longitude and transverse small deformations at the end of the samples in the different lattices that we use in this paper and then find c_R via Eq. (D1). The results are shown in Fig. 11 with the circles indicating the results with only twelve 60° angles that were taken into account and with the triangles indicating the results with all twenty-four 60° angles. The value of k_θ with all twenty-four 60° angles was chosen to reproduce the quantitative values of the model with only twelve 60° angle models.

We can see that, for both lattices, the numerical values for the wave velocities using $k_\theta = 0$ are very close to the 2D values [28] as can be calculated analytically. For larger values of k_θ, the different sound velocities are higher (≈10%–15%) than the 2D velocities [28]. In addition, we can see that the results for the sound velocities (specifically, c_R) with $k_\theta/k_r = 3.5$ with all twenty-four 60° angles are very much like the $k_\theta/k_r = 5$ with only twelve 60° angles.

[1] J. Fineberg and M. Marder, Phys. Rep. **313**, 1 (1999).
[2] L. B. Freund, *Dynamic Fracture Mechanics* (Cambridge University Press, Cambridge, UK, 1998).
[3] E. Bouchbinder, J. Fineberg, and M. Marder, Annu. Rev. Condens. Matter Phys. **1**, 371 (2010).
[4] E. Bouchbinder, T. Goldman, and J. Fineberg, Rep. Prog. Phys. **77**, 046501 (2014).
[5] M. Adda-Bedia, J. Mech. Phys. Solids **53**, 227 (2005).
[6] J. Fineberg, S. P. Gross, M. Marder, and H. L. Swinney, Phys. Rev. Lett. **67**, 457 (1991).
[7] E. Sharon, S. P. Gross, and J. Fineberg, Phys. Rev. Lett. **74**, 5096 (1995).
[8] E. Sharon and J. Fineberg, Phys. Rev. B **54**, 7128 (1996).
[9] E. Sharon and J. Fineberg, Philos. Mag. B **78**, 243 (1998).
[10] E. Sharon and J. Fineberg, Adv. Eng. Mater. **1**, 119 (1999).
[11] E. H. Yoffe, Philos. Mag. **42**, 739 (1951).
[12] J. D. Eshelby, in *Inelastic Behavior of Solids*, edited by M. F. Kanninen (McGraw-Hill, New York, 1970).
[13] L. I. Slepyan, Dokl. Akad. Nauk SSSR **258**, 561 (1981) [Sov. Phys. Dokl. **26**, 538 (1981)].
[14] S. A. Kulamekhtova, V. A. Saraikin, and L. I. Slepyan, Izv. Akad. Nauk SSSR Mekh. Tverd. Tela **19**, 112 (1984) [Mech. Solids **19**, 102 (1984)].
[15] M. Marder and X. Liu, Phys. Rev. Lett. **71**, 2417 (1993).
[16] D. A. Kessler and H. Levine, Phys. Rev. E **63**, 016118 (2000).
[17] L. Pechenik, H. Levine, and D. A. Kessler, J. Mech. Phys. Solids **50**, 583 (2002).
[18] S. I. Heizler, D. A. Kessler, and H. Levine, Phys. Rev. E **66**, 016126 (2002).
[19] S. I. Heizler and D. A. Kessler, Contin. Mech. Thermodyn. **22**, 505 (2010).
[20] M. Marder and J. Fineberg, Phys. Today **49**(9), 24 (1996).
[21] M. L. Falk, Phys. Rev. B **60**, 7062 (1999).
[22] O. Dauchot, S. Karmakar, I. Procaccia, and J. Zylberg, Phys. Rev. E **84**, 046105 (2011).
[23] I. Procaccia and J. Zylberg, Phys. Rev. E **87**, 012801 (2013).
[24] W. H. Zachariasen, J. Am. Chem. Soc. **54**, 3841 (1932).
[25] P. Y. Huang, S. Kurasch, A. Srivastava, V. Skakalova, J. Kotakoski, A. V. Krasheninnikov, R. Hovden, Q. Mao, J. C. Meyer, J. Smet, D. A. Muller, and U. Kaiser, Nano Lett. **12**, 1081 (2012).
[26] S. I. Heizler, D. A. Kessler, and H. Levine, Phys. Rev. E **84**, 026102 (2011).
[27] S. I. Heizler, D. A. Kessler, and Y. S. Elbaz, Phys. Rev. E **88**, 022401 (2013).
[28] S. I. Heizler and D. A. Kessler, Phys. Rev. E **92**, 012403 (2015).
[29] I. Kolvin, G. Cohen, and J. Fineberg, Phys. Rev. Lett. **114**, 175501 (2015).
[30] F. F. Abraham, D. Schneider, B. Land, D. Lifka, J. Skovira, J. Gerner, and M. Rosenkrantz, J. Mech. Phys. Solids **45**, 1461 (1997).
[31] F. F. Abraham, R. Walkup, H. Gao, M. Duchaineau, T. D. De La Rubia, and M. Seager, Proc. Natl. Acad. Sci. USA **99**, 5777 (2002).
[32] E. Bitzek, J. R. Kermode, and P. Gumbsch, Int. J. Fract. **191**, 13 (2015).

[33] D. A. Kessler and H. Levine, Phys. Rev. E **59**, 5154 (1999).
[34] O. Padon, Trends in Scientific Computing and GPU Computing (in Hebrew), Physics Department, Nuclear Research Center-Negev, N-11/010 (2011).
[35] C. Cooper, Boston University, lecture notes, *GPU Computing with CUDA*, UTFSM, Valparaíso, Chile (2011).
[36] J. D. Achenbach, *Wave Propagation in Elastic Solids* (North-Holland, Amsterdam, 1973).